

Distributed parameters modeling for the dynamic stiffness of a spring tube in servo valves

Xinbei Lv^a, Bijan Krishna Saha^a, You Wu^b and Songjing Li^{*}

Department of Fluid Control and Automation, Harbin Institute of Technology,
Box 3040, Science Park, No. 2, Yikuang Street Nangang District, Harbin 150001, PR China

(Received October 21, 2019, Revised February 12, 2020, Accepted February 20, 2020)

Abstract. The stability and dynamic performance of a flapper-nozzle servo valve depend on several factors, such as the motion of the armature component and the deformation of the spring tube. As the only connection between the armature component and the fixed end, the spring tube plays a decisive role in the dynamic response of the entire system. Aiming at predicting the vibration characteristics of the servo valves to combine them with the control algorithm, an innovative dynamic stiffness based on a distributed parameter model (DPM) is proposed that can reflect the dynamic deformation of the spring tube and a suitable discrete method is applied according to the working condition of the spring tube. With the motion equation derived by DPM, which includes the impact of inertia, damping, and stiffness force, the mathematical model of the spring tube dynamic stiffness is established. Subsequently, a suitable program for this model is confirmed that guarantees the simulation accuracy while controlling the time consumption. Ultimately, the transient response of the spring tube is also evaluated by a finite element method (FEM). The agreement between the simulation results of the two methods shows that dynamic stiffness based on DPM is suitable for predicting the transient response of the spring tube.

Keywords: servo-valve; distributed parameters; spring tube; transient response; mathematical model

1. Introduction

Electro-hydraulic servo valves have been one of the critical components in the hydraulic control system for more than half a century because the working performance of the entire system always relies on the characteristics of the servo valves. As one of the most widely used servo valves, the flapper-nozzle servo valve possesses many advantages, such as high-speed responsibility and output pressure. According to the special structure of the pilot stage and the high-frequency working condition, self-exciting oscillation is frequently induced during its operation, which is an important factor limiting the servo valve's wider application by breaking the spring tube. Thus, investigating the inducement of self-excited oscillation and suppressing the self-exciting oscillation are crucially significant to performance improvement of the entire servo valve.

To improve performance and avoid the self-excited oscillation of the hydrodynamic system, some researchers have already made achievements (Zhu *et al.* 2016), Amirante *et al.* (2014), Qiu *et al.* (2016)). Mchenya *et al.* (2012) simulated the flow field of the flapper-nozzle pilot stage with various inlet conditions, and the form of the flow field is obtained. Aung *et al.* (2013a, b, 2014) investigated the velocity and pressure distribution of the flow field

by an LES simulation model, compared the experiment and numerical simulation results of the location where the cavitation generated, and also analyzed the inducement of cavitation occurrences. Since both of them focused on flow field observation, the intensity of the cavitation had not receded until Zhang *et al.* (2015a, b) discovered an innovative structure of the flapper, which is a rectangular instead of elliptical. The new flapper can reduce the cavitation volume generated near the nozzle and flapper. Meanwhile, Peng *et al.* (2014) used the magnetic fluid as a linear spring and damper, and the resonance amplitudes of the torque motor can be reduced significantly after a magnetic fluid is applied. However, most of these researchers focused on the suppression of the servo valve self-excited phenomenon by changing the element of the servo valve, and none of them established any mathematical model to explain the inhibition of self-excited vibration.

Some other studies established a mathematical model (Valdés *et al.* 2007, Mu *et al.* 2011, Mesropyan and Sharipov (2016) to interpret transient motion characteristics. Somashekhar *et al.* (2007) developed a mathematical model for a jet pipe servo valve by using MATLAB and a finite element model (FEM), and an experiment was also carried out to ensure that the mathematical model was precise enough. Karunanidhi and Singaperumal (2010) designed and analyzed the multilayer piezoelectric actuator with an amplifier by the methods of finite element analysis and an experiment, and a one-dimensional mathematical model was also established to elucidate the relationship between various sections of the servo valve. Liu *et al.* (2014) investigated a seventh-order model of the servo valve that can reflect more physical behavior than the classical low-

*Corresponding author, Professor

E-mail: lisongjing@hit.edu.cn

^a Ph.D. Student

^b M.Sc. Student

order mathematical model. Compared with the AMESim simulation model, the seventh-order model was more suitable for the linear control design approach. Li (2016) developed a new mathematical model that can reflect the physical mechanism of a jet-pipe/deflector-jet valve and according to the model, the suitable diameter of the receiving hole is confirmed. Numerical simulation and experiments were also conducted, and the pressure and velocity were compared with the theoretical model, which was very approximate. As we can see, in the research field of servo valves, most of the mathematical model research has focused on one-dimensional models that can reflect the operation characteristics of servo valves. However, the limitation of a one-dimensional model is that the dynamic response of the servo valve is ignored, which is the core issue affecting self-excited oscillation.

Meanwhile, many scholars have established a mathematical model for some similar structures to obtain a dynamic response (Rihuan *et al.* 2018, Mohammadnejad and Kazemi 2018, Zhao *et al.* 2019). Chen and Yang (2016) investigated the free and forced vibration characteristics of functionally graded porous beams with the DPM. The relationship between the material slenderness ratio, natural frequency, and dynamic deflection of the beam was derived and the optimal distribution structure of the materials was inferred. Akbarov *et al.* (2019) studied the dynamics of the oscillating moving load acting in the interior of the hollow cylinder. The corresponding 3D dynamic modal is obtained by employing the moving coordinate system and the exponential Fourier is transformed and presented with the Fourier series, which establishes the link between the load oscillation, critical velocity, and the interface stress. Tlidji *et al.* (2019) developed a quasi-3D beam theory for free vibration analysis of functionally graded microbeams. The equation of motion was derived by using the DPM method and Hamilton's principle. Numerical results showed the relationship between the function distribution, power index, material scale parameter, and the fundamental frequencies of microbeams.

For establishing the relationship between the driving signal and dynamic response and finding methods to overcome the oscillations, a mathematical model based on distributed parameters is needed rather than the one-dimensional model for mechanical system. Liu *et al.* (2012a, 2012b) deduced the DPM of a manipulator handling a flexible load, and the system vibration amplitude was suppressed efficiently by the load-position control algorithm that was extracted by the DPM. Whalley R *et al.* (2015) considered a mathematical model of gas pipelines by a DPM, and a closed-loop regulation strategy for optimization was proposed. The transient response of the output that was affected by the input signals and load disturbance was presented. Babaei and Antonios (2015) built an output feedback controller for physicochemical systems by a DPM. The dynamic observer of the physicochemical systems was also designed by adaptive proper orthogonal decomposition method, which confirmed the model's precision. Omidi *et al.* (2016) investigated a DPM control method based on the integral consensus control method, and the superiority of distributed parameter

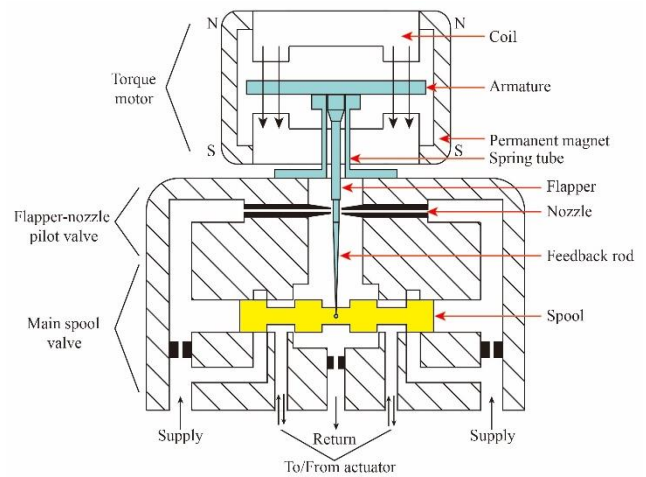


Fig. 1 Typical structure of a two-stage electro-hydraulic servo

model control was verified by the cantilever beam vibration control experiment.

It can be seen that DPM systems have been widely used in mechanical systems with simple structures, but the application of this model has encountered some difficulties in complex structures. Thus, to guarantee a certain calculation accuracy while reducing the simulation time, a mathematical model of a servo valve spring tube based on the DPM is established to calculate the dynamic stiffness of the spring pipe. Here, the DPM numerical simulation results are obtained using MATLAB2016, and the FEM numerical simulation results are achieved by ANSYS Workbench 19.2.

2. Working principle of the servo-valve

The typical structure of a two-stage electro-hydraulic servo valve using a flapper-nozzle pilot stage is shown in Fig. 1. It consists of three major parts, including the torque motor, pilot stage, and main spool. The electrical signal is converted into the mechanical motion by the torque motor, which makes the armature generate an angle of rotation. The pressure acting on the flapper by the symmetrical nozzles will be different due to the rotation of the armature. Since the two nozzles and the main spool are connected by the channel of oil, the pressure difference is delivered to the ends of the main spool. This pressure difference makes the spool move and the feedback rod also starts to distort. The deformation of the feedback rod and the pressure difference provided by the two nozzles prompt the armature to rotate back to the original position. Ultimately, the closed-loop precision control system is established by the force-displacement feedback loop.

The classical mathematical model of the armature transient dynamic response is expressed as (Aung 2015):

$$T_d = J_a \frac{d^2\theta}{dt^2} + B_a \frac{d\theta}{dt} + K_a\theta + T_{L1} + T_{L2} \quad (1)$$

where T_d is the electromagnetic torque provided by a torque motor; T_{L1} is the jet torque of two symmetric nozzles; T_{L2} is

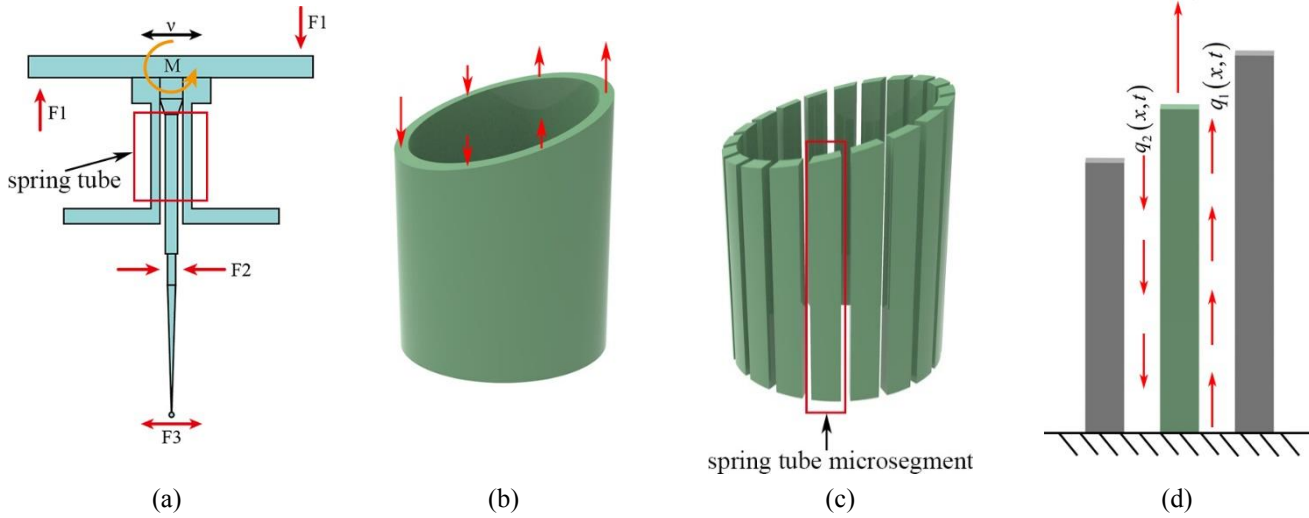


Fig. 2 Spring tube motion discrete process

the feedback torque, which is due to the movement of the main spool; J_a and B_a are the inertia moment and viscous damping coefficient of the armature; and K_a is the stiffness coefficient of the spring tube.

The transient response of the spring tube is reflected by the stiffness of the spring tube K_a , which means that the spring tube is simplified into a single-span beam and that its dynamic response is also replaced by the static torsional deformation. For observing the dynamic characteristics of spring tube deformation and analysing the relationship between the deformation and input electrical signal in the meantime, static simplification is undoubtedly far from sufficient. Thus, the dynamic mathematical model for investigating the mechanism of the armature component vibrating is urgently needed. As the first step of mathematical modelling, the spring tube, that is, the connection between the clamping surface and armature, is paramount to consider in the following section.

3. Spring tube dynamic stiffness distributed parameter mathematical model

There are three kinds of loads acting on the armature, electromagnetic force, jet force, and deformation force of feedback spring, as shown in Fig. 2(a). The armature rotates around the center of mass under the influences of these loads, and then the deformation occurs in the spring tube. For simplifying the mathematical model, the axial tensile stress of the spring tube is the paramount consideration in this paper. The spring tube is stretched and compressed along the axial direction when the axial tensile stress acts on the spring tube, as shown in Fig. 2(b). Due to the difference between the spring tube deformation along the circumference, the spring tube is dissociated into several pieces in the process of mathematical modelling, as shown in Fig. 2(c). The discrete unit of the spring tube is regarded as a single-span beam whose one end is fixed and the opposite is free. The driving forces acting on the beam unit

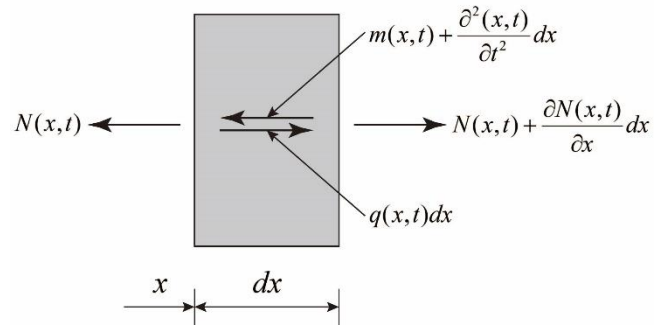


Fig. 3 Force acting on the spring tube microsegment

can be divided into two categories, the force transmitted from the armature $f(t)$ and the adjacent beam units $q_1(x,t)$ ($q_2(x,t)$ is shown in Fig. 2(d)). Under the influence of these external forces, the beam unit generates the vibration along the axial direction.

The force equilibrium equation of the beam microsegment when the axial free vibration is generated can be expressed as (Clough *et al.* 1975):

$$N(x,t) + f_1(x,t)dx - [N(x,t) + \frac{\partial N(x,t)}{\partial x}dx] - q(x,t)dx = 0 \quad (2)$$

where $q(x,t)$ is the external load, $N(x,t)$ represents the time-varying internal force along the axial direction, and $f_1(x,t)$ denotes the inertia force. The complete stress situation is shown in Fig. 3.

The first step of developing the DPM should be deriving the undamped nature mode and frequency of the microsegment vibration. According to Eq. (2), the axial free vibration equation of the spring tube microsegment can be simplified as

$$m \frac{\partial^2 u(x,t)}{\partial t^2} - \frac{\partial}{\partial x} \left[\frac{\partial u(x,t)}{\partial x} EA \right] = 0 \quad (3)$$

where m , E , and A are respectively the mass, elasticity

modulus, and cross-sectional area of the spring tube. Besides, $u(x,t)$ is the axial displacement of the microsegment that can be expressed as

$$u(x,t) = \phi(x)Y(t) \tag{4}$$

where $\phi(x)$ and $Y(t)$ are respectively the mass normalized eigenfunction and modal mechanical response expressions. The particular solution of $\phi(x)$ can be obtained as follows:

$$\phi(x) = C_1 \cos\left(\omega\sqrt{\frac{m}{EA}}x\right) + C_2 \sin\left(\omega\sqrt{\frac{m}{EA}}x\right) \tag{5}$$

where C_1 and C_2 are constants whose algebraic relationship can be obtained by the boundary condition of the spring tube microsegment and ω represents the natural frequency of the microsegment. The deflection of the microsegment fixed end is zero, and the force acting on the free end is also zero. Thus, we can obtain

$$\phi(0) = 0 \quad N(L) = EA\phi'(L) = 0 \tag{6}$$

After simplification, the formation function of spring tube microsegment will be

$$\phi_n = C_2 \sin\left[\frac{\pi}{2L}(2n-1)x\right] \tag{7}$$

Here, C_2 can be an arbitrary value, but each value corresponds to a unique amplitude function. To simplify the calculation, C_2 takes the value of 1. The subscript n denotes the nominal modes. The height of the microsegment L is 5.533 mm. Finally, Eq. 7 turns into

$$\phi_n = \sin[283.8959 \times (2n-1)x] \tag{8}$$

With the material properties of the spring tube shown in Table 1, the natural frequency of the microsegment could be obtained. At the same time, to verify the validity of the mathematical model for modal prediction, the nature frequency could also be predicted by the FEM, and a comparison of the results of the two methods is plotted in Table 2. Moreover, the corresponding mode shapes are given in Fig. 4, in which (a) to (d) denote the first four modes, respectively. For the spring tube microsegment, the mode predicted by the DPM showed little difference compared with the FEM simulation results, and the maximal relative error occurring in the first mode was 0.82%. The harmonic response simulated by the FEM is plotted in Fig. 5, and the first three modes shapes predicted by the DPM are marked. It is obvious that the DPM did not miss any natural frequencies during the modal prediction process.

The DPM system has an infinite number of modes. According to the principle of shape superposition, the prediction of the DPM system will be accurate enough by only using several modes whose frequencies are close to the actual working condition. The first natural frequency of the microsegment is 174938 Hz, which is much higher than the actual operating frequency. Thus, the process of vibration is

Table 1 Armature component material properties

Section	Material	Density ρ (kg/m ³)	E(GPa)	Poisson's ratio μ
Spring tube	QBe1.9	8230	125	0.35

Table 2 Numerical comparison of the nature frequency prediction

Mode	Nature Frequency(Hz)		
	Matlab	Ansys	Relative Error
1	174938	176380	0.82%
2	524814	528830	0.76%
3	874690	880380	0.65%
4	1224566	1230300	0.47%

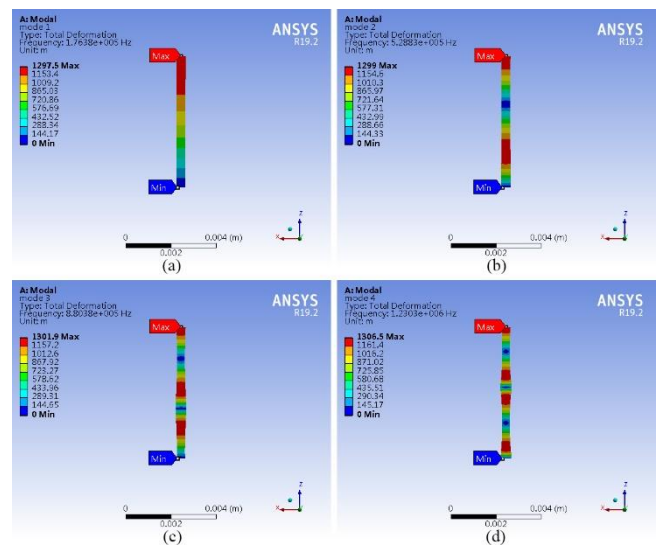


Fig. 4 The first fourth modes of spring tube microsegment simulated by FEM

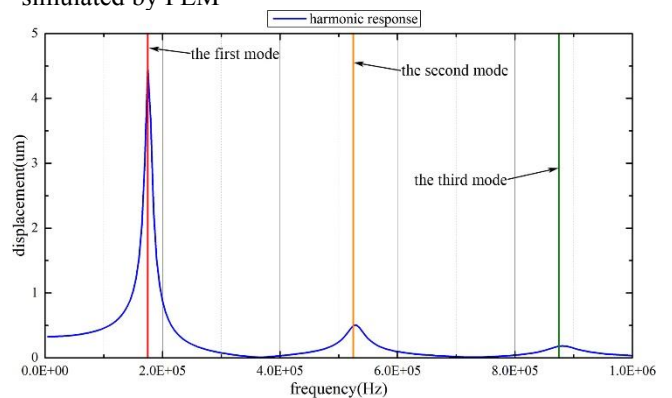


Fig. 5 The spring tube microsegment harmonic response

mainly constituted by the first-order mode. For saving the simulation resources, only the first and third mode of vibration were considered in the subsequent simulation process. Finally, the relationship between time, coordinate position, and the deflection of spring tube at any position could be expressed as

$$u(x,t) = \sum_{i=1}^3 \phi_i(x)Y_i(t) \tag{9}$$

Considering the influence of viscous damping, the time-varying internal force turns into

$$N(x,t) = A(x)\sigma(x,t) = (\varepsilon(x,t) + a_0\dot{\varepsilon}(x,t))EA(x) = \left(\frac{\partial u(x,t)}{\partial x} + a_1 \frac{\partial^2 u(x,t)}{\partial x \partial t} \right) EA(x) \quad (10)$$

With the resistance to the longitudinal speed, which is given as

$$f_D(x,t)dx = a_0 m(x) \frac{\partial u(x,t)}{\partial t} dx \quad (11)$$

where a_0 and a_1 are constant.

With the external force, Eq. 3 turns into

$$m \frac{\partial^2 u(x,t)}{\partial t^2} + a_0 m(x) \frac{\partial u(x,t)}{\partial t} dx - \left(\frac{\partial^2 u(x,t)}{\partial x^2} + a_1 \frac{\partial^3 u(x,t)}{\partial x^2 \partial t} \right) EA = q(x,t) \quad (12)$$

Assuming that the deflection of the n-th mode can be expressed as

$$v_n(x,t) = \phi_n(x) \rho_n \sin(\omega_n t + \phi_n) \quad (13)$$

Them, with Eq. 13, Eq. 3 turn into

$$\omega_n^2 m(x) \phi_n(x) = - \frac{d}{dx} \left[EA \frac{d\phi_n}{dx} \right]. \quad (14)$$

By substituting Eq. (9) and (14) into Eq. (12), we obtain

$$\sum_{i=1}^3 m(x) \phi_i(x) \ddot{Y}_i(t) + \dot{Y}_i(t) (a_0 m \phi_i(x) + a_1 m \omega_i^2 \phi_i(x)) + m \omega_i^2 \phi_i(x) Y_i(t) = q(x,t) \quad (15)$$

Each item is multiplied by $\phi_n(x)$ and integrated. Due to the orthogonality of different modes, the product of different frequency modes is 0. With the generalized mass and generalized load that can be obtained by

$$M_n = \int_0^L m(x) \phi_n^2(x) dx \quad (16a)$$

$$P_n = \int_0^L \phi_n(x) q(x,t) dx \quad (16b)$$

Then we obtain the axial motion equation of the spring tube microsegment that can be expressed as

$$M_n \ddot{Y}_n(t) + \dot{Y}_n(t) (a_0 + a_1 \omega_n^2) M_n + \omega_n^2 M_n Y_n(t) = P_n(t) \quad (17)$$

Assuming that ξ_n is the Rayleigh damping ratio of the n-th mode, then it can be expressed by

$$\xi_n = \frac{a_0}{2\omega_n} + \frac{a_1 \omega_n}{2} \quad (18)$$

where ξ_1 and ξ_9 are valued as 0.45 according to experience. By Eq. (18), we obtain $\xi_2 = 0.217$ and $\xi_3 = 0.135$. Then, Eq. (17) becomes

$$M_n \ddot{Y}_n(t) + \omega_n \xi_n M_n \dot{Y}_n(t) + \omega_n^2 M_n Y_n(t) = P_n(t) \quad (19)$$

The generalized load contains two forces, the shear forces transmitted from adjacent sides and the axial force transmitted by the armature, which can be expressed as

$$P_n = \int_0^L q(x,t) \phi_n(x) dx = b \times N_0 \times \phi_n(L) + \int_0^L \left(\left(\phi_n(x) Y_n(t) - \phi_{n-1}(x) Y_{n-1}(t) \right) \times G \times \phi(x) \right) dx \quad (20)$$

where b is 1 when the mode is odd and -1 when the mode is even, $\phi_n(x) Y_n(t) - \phi_{n-1}(x) Y_{n-1}(t)$ is the relative displacement of target and adjacent microsegments at the height of x, G is the shear modulus of elasticity which can be obtained by $G = E / (2(1 + \mu))$, and μ is the Poisson's ratio of the spring tube.

Then, Eq. (19) turns into a second-order differential equation by which $Y_n(t)$ can be solved. With the function of mode shape $\phi(x)$ and $u(x,t)$ obtained by Eq. (14), the movement equation of the spring tube microsegment is obtained. After the time step is properly dispersed, the dynamic response of the spring tube microsegment based on the DPM dynamic stiffness can be calculated. Finally, by using the software MATLAB, the dynamic response of each microsegment and the entire spring tube can be obtained.

4. Numerical simulation

4.1 Numerical simulation verification of the spring tube microsegment based on the DPM

To verify the dynamic stiffness mathematical model of the spring tube microsegment, the dynamic response of the microsegment under different transient external loads was simulated. Meanwhile, the result was also obtained by the FEM numerical simulation as plotted in Fig. 6, which shows the deformation response curve of the microsegment above. The external load was tentatively a sinusoidal signal with an amplitude of 0.2 N and a frequency of 800 Hz. The two simulation results show little difference. The deformation curve predicted by the DPM had a certain lag behind the FEM prediction result, and the amplitude of the DPM deformation curve was also smaller than the FEM by 13.5%, which may be caused by the setting error of the damping coefficient.

The verification of another common input signal square wave is represented in Fig. 7 with the same amplitude but a higher frequency of 2500Hz. It shows that, after changing the direction of the input signal, the dynamic response of the DPM was delayed compared with the FEM by 0.04 ms when the spring tube displacement reached a stable position. Due to the limitation of the working environment, the vibration frequency of the spring tube would not exceed 5000 Hz, which ensures that the mathematical model simulation result reached the equilibrium position before the signal transformation. This phenomenon may be improved if the Rayleigh damping ratio is increased to an appropriate value. The equilibrium position predicted by the mathematical model simulation was lower than that of FEM

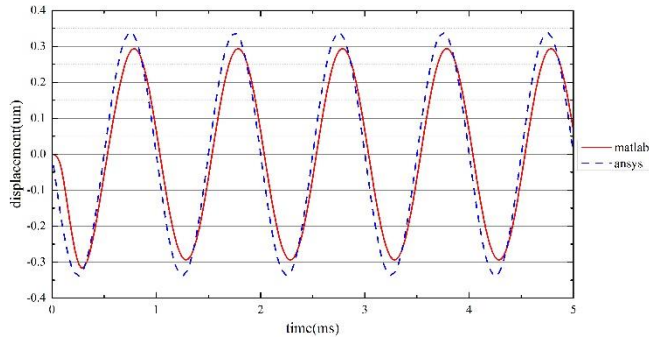


Fig. 6 Sinusoidal signal simulation verification

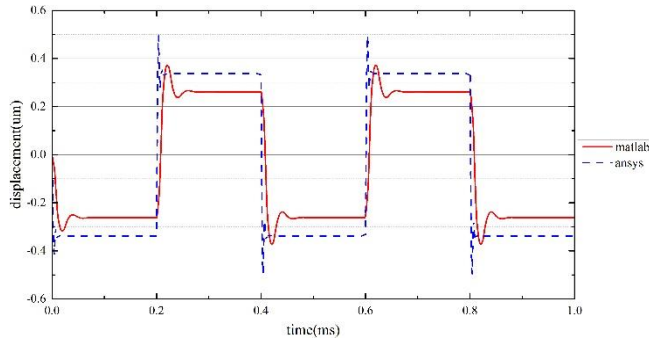


Fig. 7 Square signal simulation verification

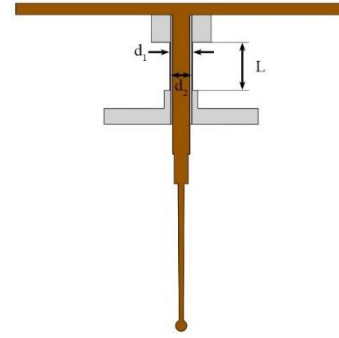


Fig. 8 Spring tube structure

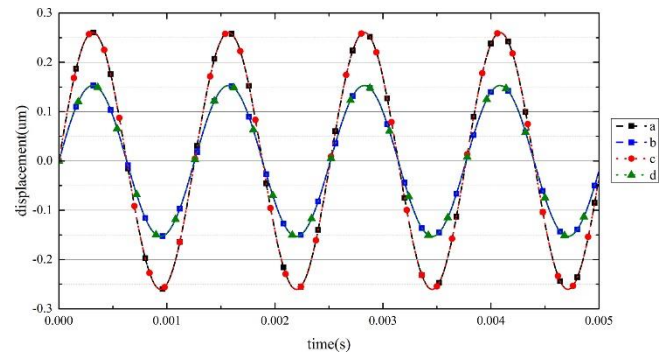


Fig. 9 Simulation area comparison

by 22%, which may be induced by the calculation error of a higher generalized stiffness (calculated by $\omega_n^2 M_n$). Since the natural frequency of spring tube was verified in previous work, the cause of this error was mainly caused by the calculation process of generalized mass.

4.2 Dynamic stiffness numerical simulation based on DPM

The numerical simulation program was written depending on the structure of the spring tube, as shown in Fig. 8. The length L of the spring tube was 5.533 mm and the horizontal section was a ring with a 2.472 mm inner diameter (d_2) and 2.6 mm outer diameter (d_1). The driving force transmitted by the armature was simplified to a dynamic load acting on the top side of spring tube with the expression $p(x,t)=ax \cdot \sin(b \cdot t)$, x is the horizontal distance between the load location and the rotation center of spring tube, a is the load amplitude with the value 12693822475, b is the frequency whose value is 5000, and the coefficient t is the simulation time set according to previous works (Peng 2015b).

Aiming at seeking a suitable program, different types of simulation programs were attempted. To reduce the time consumption of numerical simulation, the spring tube structure involved in the calculation was first simplified. Since the spring tube deformation is symmetrical along the armature rotation plane, it was only necessary to simulate half of the spring tube. Two methods of simplification were attempted that involved half and a quarter spring tube. The spring tube microsegment located in the max positive deformation place was named the No.1 microsegment. As the circumferential distance from the maximum point to the

microsegment increased, the spring tube number decreased, and the subsequent microsegment was named after this. The displacement curves of the different spring tube microsegments are plotted in Fig. 9, where lines a and c respectively represent the first and fourth segment end displacement simulated by a quarter spring tube programs, and b and d belong to programs with half spring tube. The distinction between the two curves is tiny while the time consumption of the half spring tube simulation was almost twice that of the one quarter method. Therefore, only a quarter of the spring tubes were simulated in the following numerical simulation program.

The number of spring tube microsegments dispersed in a quarter spring tube has a serious impact on the accuracy of the simulation results. Therefore, different microsegment numbers involved in a quarter spring were simulated by diverse programs. The displacement curves of the first microsegment end that were obtained by these programs are shown in Fig. 10(a) (the microsegment numbers are 1, 3, 5, 10, and 20, separately). Under the excitation of the sinusoidal driving force, the deformation curve of the microsegment end is in the form of a sinusoid. The vibration period of different curves is equivalent while the amplitude of those curves is different. The difference between these curves can be easily detected in Fig. 10(b) during the physical time from 9.4ms to 10ms. The vibration amplitudes with only one segment and three segments are significantly different from the amplitudes of the other segment numbers. The amplitude of one segment is 0.2361 μm , that of the three segments is 0.2706 μm , and the amplitude of the remaining curves is basically the same with about 0.2612 μm . The amplitude numerical values and computational time consumption of the diverse

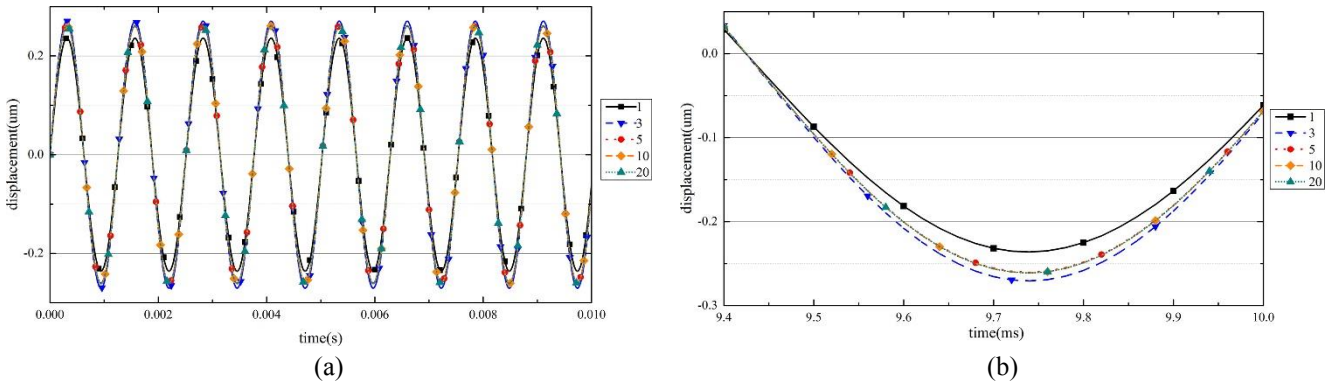


Fig. 10 Spring tube microsegment end displacement of the different microsegments number

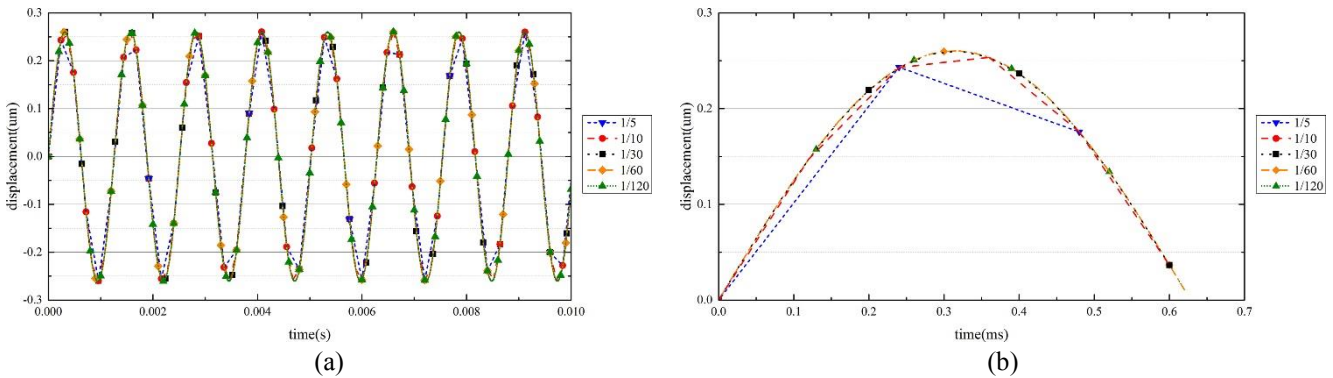


Fig. 11 Spring tube microsegment end displacement of different time step

Table 3 Simulation numerical result of different microsegment numbers

microsegment number	1	3	5	10	20
amplitude(μm)	0.2361	0.2706	0.2603	0.2611	0.2612
relative error	9.61%	3.62%	0.33%	0.02%	/
simulation time(min)	5.67	17.18	30.63	81.13	208.68

microsegments numbers programs are listed in Table 3, and the relative error of the different programs is listed showing a comparison with the results of the program with 20 microsegments. As shown, the time consumption increased significantly while the number of microsegments increased, and the relative error decreased sharply before the microsegment number reached 5. Hence, to guarantee the simulation accuracy while controlling the time consumption, the microsegment was determined by 5 pieces in the following program.

Furthermore, the time step size of the simulation program was also one of the key factors affecting the accuracy of the numerical simulation. Since the choice of time step depends on the period of the excitation force, different time steps (1/5, 1/10, 1/30, 1/60, and 1/120 of the excitation force period) were attempted to seek the suitable proportion by the various programs. The displacement curves of the first spring tube microsegment end are plotted in Fig. 11(a). All the displacement curves of the different time steps are sinusoidal waves, and the distinction between the amplitude of the different curves is also pinging. The

displacement curves are magnified in Fig. 11(b) during the physical time between 0 ms - 0.7 ms, and the curves of the time step are 1/5 and 1/10 of the driving force period, which are different compared with the remaining curves caused by the lack of an intermediate amount. After the time step declined to 1/30 of the driving force period, only a slight difference can be seen. Meanwhile, the computational time was approximately inversely proportional to the time step. Hence, to seek a balance between the numerical accuracy and computational recourses, the time step of 1/30 of the driving force period was selected for all the following simulation programs.

4.3 Numerical simulation verification

For confirming the validity of the dynamic stiffness model based on the DPM, the numerical simulation results were obtained by the FEM under the same condition as the previous numerical simulation. The verification was conducted by comparing the DPM and FEM numerical simulation results. The 3-dimensional geometry of the spring tube is shown in Fig. 12. The mesh had 12519 cells in total with a basic element size of 1 mm.

According to the working conditions of the servo valve, the bottom of the spring tube base was set as a fixed support. The driving force transmitted by the armature was the same as the previous simulation program, as shown in Fig. 13. Since the electromagnetic signals appeared in a sinusoidal and square waveform during the operation of the servo valve, the form of the driving force in the simulation process was only the sinusoidal and square wave signal.

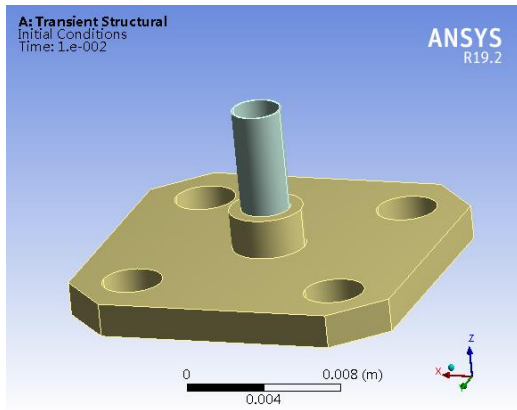


Fig. 12 Workbench simulation model and mesh

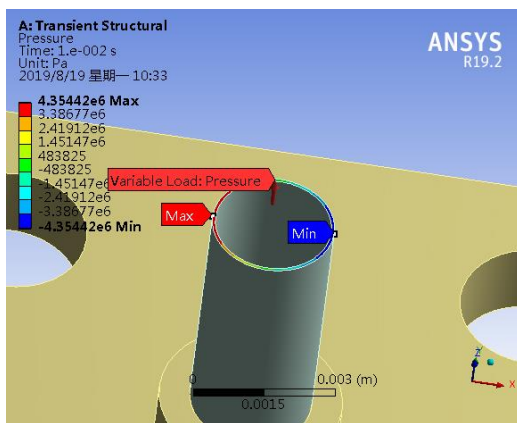


Fig. 13 Dynamic load acting on the spring tube

The other simulation environment was set according to the previous simulation program, including the material properties of the spring tube and so on.

The numerical simulation results obtained by the two different methods with the sinusoidal driving force were compared to determine the validity of the mathematical model, as shown in Fig. 14. Fig. 14(a) represents the deformation comparison results of the first spring tube microsegment end and Fig. 14(b) and (c) show the results of the third and fifth microsegments. All the deformation curves present a regular sine wave determined by the sinusoidal driving force while the amplitude of the curves has a certain difference.

A verification of different simulation methods with the driving force in the square wave was also conducted. The frequency of the square wave rose to 5000 Hz, which is the upper limit of the servo-valves working frequency. Fig. 14(d), (e), and (f) respectively present the first, third, and fifth spring tube microsegment deformations. After the step signal intervened in the system, the response of the DPM was faster than that of the FEM, the time consumption of the DPM for reaching the equilibrium position was also less, and the static position predicted by the two methods shows a good agreement while the relative error was 5.98%.

The frequency-domain analysis results of the spring tube microsegment deformation with the frequency between 0 to 6000 Hz, covering the operating frequency range of the servo valves, is shown in Fig. 15. This figure shows the

Table 4 Numerical comparison of the simulation results

Spring tube number	Matlab(um)	Ansys(um)	Relative Error
1	0.25899	0.20749	19.88%
2	0.24858	0.19716	20.68%
3	0.21473	0.16775	21.87%
4	0.15988	0.12184	23.79%
5	0.0891	0.06408	28.81%

comparative results of the first spring tube microsegment end maximum deformation during the simulation, where the sampling frequency was 200 Hz and the driving force was sinusoidal. The program of dynamic stiffness mathematical model was also adjusted according to the frequency-domain analysis, which calculates the maximum deformation of the microsegment end during the simulation. It is obvious that the two curves remain almost unchanged, and the difference in the driving force frequency had little effect on the amplitude of deformation. The first microsegment deformation amplitude of the mathematical model simulation was smaller than that of the FEM by 19.88%, and the distinction kept rising as the microsegment number increased, which reached 28.81% at the fifth microsegment (as shown in Table 4).

The driving force frequency that caused the spring tube deformation was much lower than the first-order vibration frequency calculated by the mathematical model, which indicates that the spring tube mainly reflects the first-order vibration mode when it vibrates. This is also confirmed by the phenomenon that the harmonic response curves of the DPM and FEM numerical simulation results nearly remained constant. The error between the mathematical model simulation and the FEM may be due to the negligence of the tangential displacement of the spring tube and the calculation error in establishing the mathematical model. As the spring tube microsegment number increased, the relative displacement on both sides of the spring tube microsegment became larger and the shear stress increased accordingly. Meanwhile, the difference between the other terms in the mathematical model is indistinguishable. This is the reason that the calculation error of relative force may be the main inducement to increases in error as the spring tube microsegment number rises.

Comparing the numerical simulation results of single microsegment and the entire spring tube when the driving force was a square force, the responding speed of the DPM increased. This should also be the cause of the relative force calculation error. A relatively small interaction force will cause the microsegment to respond more quickly, and the fluctuation when reaching the equilibrium position will also disappear more quickly. Hence, correcting the interaction force will be the main task in subsequent work.

5. Conclusions

An innovative dynamic stiffness mathematical model based on distributed parameters is proposed to predict the axial deformation of the flapper-nozzle servo-valve spring

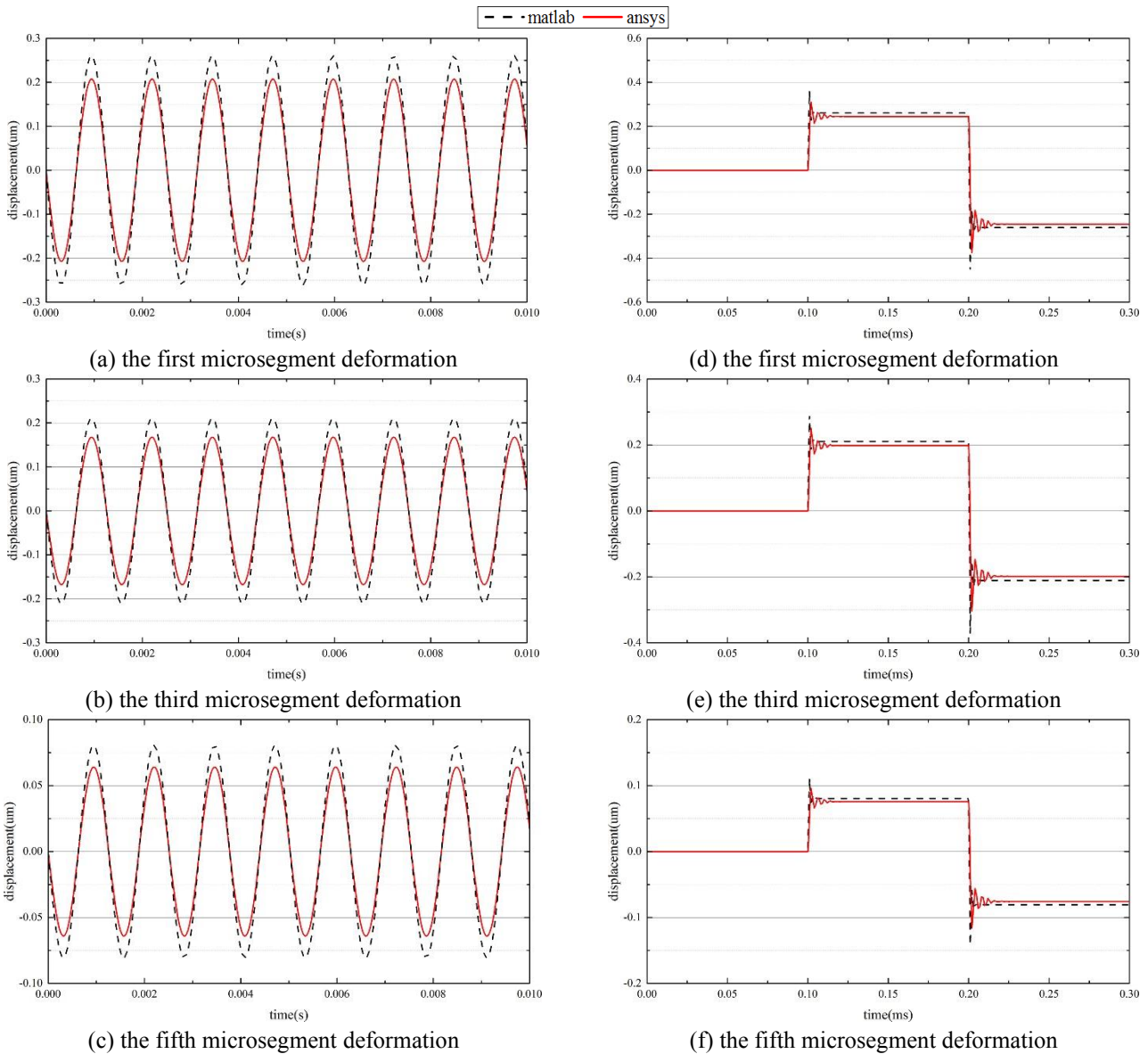


Fig. 14 Time-domain simulation results of the spring tube deformation

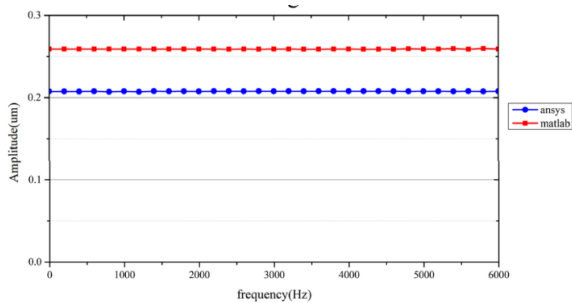


Fig. 15 Amplitude comparison of spring tube deformation

tube. The spring tube is discrete into a plurality of microsegments according to the external force transmitted from the armature and the transient response equation is derived by the method of a distributed parameter according to the boundary condition and external load. For verifying the mathematical model, a comparison of model prediction was simulated results was conducted, which showed a good agreement with the biggest error being 0.82%.

Subsequently, the simulation methods of the entire spring tube were discussed and a suitable method that can balance the calculation accuracy and calculation time was obtained.

Aimed at verifying the transient response prediction of the spring tube predicted by the mathematical model, a numerical simulation of the dynamic stiffness mathematical model and finite element method was carried out, which showed a good agreement when the driving force was sinusoidal and a square wave signal. Meanwhile, the sinusoidal driving forces at different frequencies were simulated to test the validity of the mathematical models, and the results showed that the first mode of spring tube microsegment dominated the deformation process of the spring tube. This was also confirmed by the theoretical calculation result. The reason for the error was also analyzed to include the neglect of tangential deformation, calculation error, and so on. Thus, for optimizing the mathematical model to match the simulation results of other commercial software, the influence of the tangential

deformation in the spring tube vibration and the optimization of relative force calculation should be further investigated in future work.

Acknowledgments

The work represented in this paper is supported by National Natural Science Foundation of China – China (Grant No. 51675119).

References

- Andrianov, I. V., Awrejcewicz, J. and Manevitch, L. I. (2013), *Asymptotical Mechanics of Thin-Walled Structures*, Springer Science and Business Media, Berlin, Germany.
- Akbarov, S.D. and Mehdiyev, M.A. (2019), “3D Dynamics of the Oscillating-Moving Load Acting in the Interior of the Hollow Cylinder Surrounded with Elastic Medium”, *Struct. Eng. Mech.*, **71**(6), 713-738. <https://doi.org/10.12989/sem.2019.71.6.713>.
- Amirante, R., Distaso, E. and Tamburrano, P. (2014), “Experimental and numerical analysis of cavitation in hydraulic proportional directional valves”, *Energy Conversion Manag.*, **87**, 208-219. <https://doi.org/10.1016/j.enconman.2014.07.031>.
- Aung, N.Z. and Li, S. (2013a), “A numerical study of cavitation phenomenon in a flapper-nozzle pilot stage of an electrohydraulic servo-valve with an innovative flapper shape”, *Energy Conversion Manag.*, **77**, 31-39. <https://doi.org/10.1016/j.enconman.2013.09.009>.
- Aung, N.Z., Yang, Q., Chen, M. and Li, S. (2014), “CFD analysis of flow forces and energy loss characteristics in a flapper-nozzle pilot valve with different null clearances”, *Energy Conversion Manag.*, **83**, 284-295. <https://doi.org/10.1016/j.enconman.2014.03.076>.
- Aung, N.Z. (2015), “A study of flow-induced phenomena in a flapper-nozzle pilot valve by using different innovative flapper shapes”, Ph.D. Dissertation, Harbin institute of technology, Harbin, China.
- Babaei, P.D. and Antonios, A. (2015a), “Design of APOD-based switching dynamic observers and output feedback control for a class of nonlinear distributed parameter systems”, *Chem. Eng. Sci.*, **136**, 62-75. <https://doi.org/10.1016/j.ces.2015.02.032>.
- Chen, D. and Yang, J. (2016), “Sritawat Kitipornchai. Free and forced vibrations of shear deformable functionally graded porous beams”, *J. Mech. Sci.*, **108-109**, 14-22. <http://dx.doi.org/10.1016/j.ijmecsci.2016.01.025>.
- Clough, R. and Penzien, J. (1975), “Dynamics of structures”, McGraw-Hill Inc, New York, NY, USA.
- Karunanidhi, S. and Singaperumal, M. (2010), “Mathematical modelling and experimental characterization of a high dynamic servo valve integrated with piezoelectric actuator”, *Syst. Control Eng.*, **224**(4), 419-435. <https://doi.org/10.1243/09596518jsce899>.
- Li, Y. (2016), “Mathematical modelling and characteristics of the pilot valve applied to a jet-pipe/deflector-jet servovalve”, *Sensors Actuators A Phys.*, **245**, 150-159. <https://doi.org/10.1016/j.sna.2016.04.048>.
- Li, S., Aung, N.Z., Zhang, S., Cao, J. and Xue, X. (2013b), “Experimental and numerical investigation of cavitation phenomenon in flapper-nozzle pilot stage of an electrohydraulic servo-valve”, *Comput. Fluids*, **88**, 590-598. <https://doi.org/10.1016/j.compfluid.2013.10.016>.
- Liu, C. and Jiang, H. (2014), “A seventh-order model for dynamic response of an electro-hydraulic servo valve”, *Chinese J. Aeronautics*, **27**(6), 1605-1611. <https://doi.org/10.1016/j.cja.2014.10.029>.
- Liu, S., Liu, K. and Li, Y. (2012a), “A new sliding mode control of manipulator handling a flexible payload based on distributed parameter system”, *The 31th Chinese Control Conference*, Hefei, China, July.
- Liu, S., Wang, Z., Qiao, Y., Xie, M. and Li, Y. (2012b), “An energy-based position control and asymptotic stability analysis for manipulator handling a flexible payload”, *Proceedings of 10th World Congress on Intelligent Control and Automation*, Beijing, China, June. <https://doi.org/10.1109/wcica.2012.6359074>.
- Mchenya, J.M., Zhang, S.Z. and Li, S.J. (2012), “Visualization of flow-field between the flapper and nozzle in a hydraulic servo-valve”, *Adv. Metallurgical Mining Eng.*, **402**, 407-411. <https://doi.org/10.4028/www.scientific.net/amr.402.407>.
- Mesropyan, A.V. and Sharipov, R.R. (2016), “Mathematical Modeling of Transient Processes in the Jet Pipe Servoactuator with a Dual-Mode Controller”, *Procedia Eng.*, **150**, 168-172. <https://doi.org/10.1016/j.proeng.2016.06.742>.
- Mohammadnejad, M. and Kazemi, H.H. (2018), “A new and simple analytical approach to determining the natural frequencies of framed tube structures”, *Struct. Eng. Mech.*, **65**(1), 111-120. <https://doi.org/10.12989/sem.2018.65.1.111>.
- Mu, D. and Li, C. (2011), “A new mathematical model of twin flapper-nozzle servo valve based on input-output linearization approach”, *Artificial Intelligence, Management Science and Electronic Commerce (AIMSEC)*, Beijing, China, August. <https://doi.org/10.1109/AIMSEC.2011.6009893>.
- Omidi, E.S. and Mahmoodi, N. (2016), “Vibration suppression of distributed parameter flexible structures by Integral Consensus Control”, *J. Sound Vib.*, **364**, 1-13. <https://doi.org/10.1016/j.jsv.2015.11.020>.
- Peng, J., Li, S. and Han, H. (2014), “Damping properties for vibration suppression in electrohydraulic servo-valve torque motor using magnetic fluid”, *Appl. Phys. Lett.*, **104**(17), 171905. <https://doi.org/10.1063/1.4875029>.
- Peng, J. (2015), “Study on self-excited vibration characteristics of armature assembly in a hydraulic servo valve”, Ph.D. Dissertation, Harbin institute of technology, Harbin.
- Qiu, T., Song, X., Lei, Y., Liu, X., An, X. and Lai, M. (2016), “Influence of inlet pressure on cavitation flow in diesel nozzle”, *Appl. Thermal Eng.*, **109**, 364-372. <https://doi.org/10.1016/j.applthermaleng.2016.08.046>.
- Lu, R., Liu, X., Chen, S., Xu, Z., Hu, X. and Liu, L. (2018), “Theoretical investigation on the crushing performances of Tailor Rolled Tubes with continuously varying thickness and material properties”, *J. Mech. Sci.*, **151**, 106-117. <https://doi.org/10.1016/j.ijmecsci.2018.09.012>.
- Somashekhar, S.H., Singaperumal, M. and Kumar, R.K. (2007), “Mathematical modelling and simulation of a jet pipe electrohydraulic flow control servo valve”, *Syst. Control Eng.*, **221**(3), 365-382. <https://doi.org/10.1243/09596518jsce238>.
- Tlidji, Y., Zidour, M., Draiche, K. and Safa, A. (2019), “Vibration analysis of different material distributions of functionally graded microbeam”, *Struct. Eng. Mech.*, **69**(6), 637-649. <https://doi.org/10.12989/sem.2019.69.6.637>.
- Valdés, J.R., Miana, M.J., Nunez, J.L. and Pütz, T. (2008), “Reduced order model for estimation of fluid flow and flow forces in hydraulic proportional valves”, *Energy Conversion Manag.*, **49**(6), 1517-1529. <https://doi.org/10.1016/j.enconman.2007.12.010>.
- Whalley, R. and Abdul-Ameer, A. (2015), “Gas pipeline modelling and control”, *Proceedings of The Institution of Mechanical Engineers Part C-Journal of Mechanical Engineering Science*, **229**(18), 3320-3340. <https://doi.org/10.1177/0954406215570698>.
- Zhang, S., Aung, N.Z. and Li, S. (2015a), “Reduction of undesired lateral forces acting on the flapper of a flapper-nozzle pilot valve by using an innovative flapper shape”, *Energy Conversion Manag.*, **106**, 835-848.

<https://doi.org/10.1016/j.enconman.2015.10.012>.

- Zhang, S. and Li, S. (2015b), "Cavity shedding dynamics in a flapper–nozzle pilot stage of an electro-hydraulic servo-valve: Experiments and numerical study", *Energy Conversion Manag.*, **100**, 370-379. <https://doi.org/10.1016/j.enconman.2015.04.047>.
- Zhao, J., Choe, K., Zhang, Y., Wang, A., Lin, C. and Wang, Q. (2019), "A closed form solution for free vibration of orthotropic circular cylindrical shells with general boundary conditions." *Compos. Part B Eng.*, **159**, 447–460 <https://doi.org/10.1016/j.compositesb.2018.09.106>.
- Zhu, Y., Yang, X. and Fu, T. (2016), "Dynamic modeling and experimental investigations of a magnetostrictive nozzle-flapper servovalve pilot stage", *Proceedings of the Institution of Mechanical Engineers, Part I: J. Syst. Control Eng.*, **230**(3), 244-254. <https://doi.org/10.1177/0959651815621668>.

PL